Special Issue on Selected Emerging Trends in Terahertz Science and Technology

Generalized Analysis of Output-Power Limitations of Resonant-Tunnelling-Diode Oscillators With Symmetrical Slot Antennas

Gabriele Picco, Petr Ourednik, Dinh Tuan Nguyen, and Michael Feiginov

***Abstract*—In this article, we present optimization results for the symmetrical-slot-antenna resonant-tunnelling-diode (RTD) oscillators with account of relevant antenna losses and RTD parasitics. The results are in good agreement with available experimental data. The frequency roll-off of the output power has a complicated dependence on the oscillator parameters and does not exhibit a distinct dominant mechanism responsible for it. However, the roll-off is much steeper for lower-current-density RTDs, with much better performance of high-current-density RTDs not only at terahertz (THz) but also at sub-THz frequencies. The required minimum RTD-mesa area for optimized oscillators remains in an acceptable range for common fabrication technology: ≈ 0.1–$0.2\ \mu\mathrm{m}^2$.**

***Index Terms*—Oscillators, output power, resonant-tunneling diodes, slot antenna, terahertz (THz) sources.**

I. Introduction

WHAT was once known as the terahertz (THz) gap is now home to an increasing number of technologies, coming from the fields of both electronics and photonics [1], [2]. In this context, resonant-tunnelling-diode (RTD) oscillators have gained prominence as compact and coherent THz sources capable of reaching the highest working frequencies (1.98 THz, fundamental frequency) among active electronic devices to date [3], [4], [5], [6], [7]. For comparison, the highest $f_{\max}$ for transistors is in the range of 1–1.5 THz [8], [9]. Nevertheless, the output power of RTD oscillators still needs to be significantly increased for practical applications. We know from experience that the output power of RTD oscillators steadily drops with frequency [6], [7]. For standalone oscillators, the output power drops from ≈ 0.5 mW at ≈ 100 GHz [10] to some tens of μW at ≈ 1 THz [11], [12], [13], [14] and further to $\sim \mu$W level at ~ 2 THz [4], [5]. However, there is no clarity on which mechanisms are responsible for the power decrease, whether there is a universal power law with a certain corner frequency describing it, what would be this corner frequency, what are the most crucial parameters responsible for the power drop, whether they are related to RTDs or resonator/antenna, etc. That is a circle of questions that still need to be clarified.

Moreover, one can encounter a number of disputable answers to these questions, e.g., RTD contact resistance represents the main limitation to the RTD operating frequencies and their output power, or high sub-THz/THz output power could be achieved with low-current-density RTDs. We disprove these hypotheses in this article.

In this article, we are attempting to answer the questions stated above for a particular type of RTD oscillator, namely, for symmetrical-slot-antenna RTD oscillators on InP (indium phosphide) substrates (mounted on top of Si lenses) [4], [5], [6], [7], [15], [16]. That is an important, most-basic type of RTD oscillator. Particularly, the state-of-the-art performance in terms of the output power emitted by a standalone oscillator into free space at certain frequencies and the highest operating frequency have been demonstrated with this type of RTD oscillator [4], [5], [10], [12]. With this study, we are trying to identify the general traits responsible for the decrease of the oscillator output power with frequency. These traits are likely to be similar also for more complicated oscillators (e.g., with asymmetrical slots, patch, or ring antennas, etc. [14], [17], [18], [19], [20], [21]), although their analysis goes beyond the scope of this article.

A record output power of ≈ 10 mW was recently reported at ≈ 450 GHz for an RTD array [21], and the use of array oscillators is likely to be unavoidable if the targeted output power level is beyond ≈ 1 mW [10]. Nevertheless, the arrays are built from single oscillators, and identifying the limitations

Manuscript received 11 March 2024; revised 10 June 2024; accepted 17 July 2024. Date of publication 30 July 2024; date of current version 5 September 2024. This work was supported in part by Austrian Science Fund (FWF) under Grant P30892-N30 and in part by TU Wien Bibliothek through its Open Access Funding Program. *(Gabriele Picco and Petr Ourednik contributed equally to this work.) (Corresponding author: Michael Feiginov.)*

Gabriele Picco, Petr Ourednik, and Michael Feiginov are with the Department of Electrical Engineering and Information Technology, Technische Universität Wien, 1040 Vienna, Austria (e-mail: gabriele.picco@tuwien.ac.at; petr.ourednik@tuwien.ac.at; michael.feiginov@tuwien.ac.at).

Dinh Tuan Nguyen was with the Department of Electrical Engineering and Information Technology, Technische Universität Wien, 1040 Vienna, Austria. He is now with the Faculty of Radio-Electronic Engineering, Le Quy Don Technical University, Hanoi 100000, Vietnam (e-mail: tuannd_hv@lqdtu.edu.vn).

Color versions of one or more figures in this article are available at https://doi.org/10.1109/TTHZ.2024.3435464.

Digital Object Identifier 10.1109/TTHZ.2024.3435464

© 2024 The Authors. This work is licensed under a Creative Commons Attribution 4.0 License. For more information, see https://creativecommons.org/licenses/by/4.0/

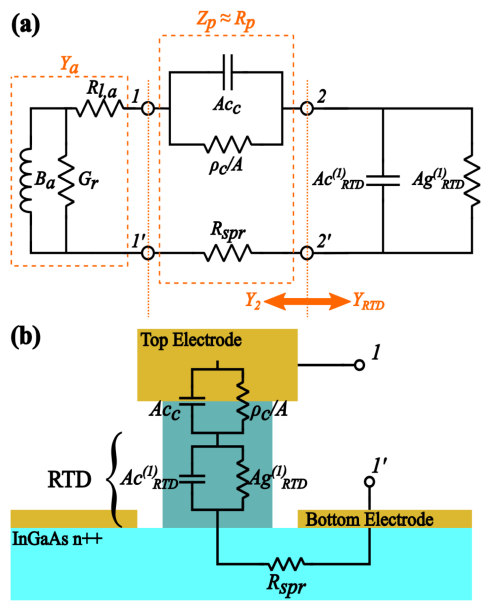

Fig. 1. (a) AC equivalent circuit of an RTD oscillator. An RTD with admittance Y_{RTD} is to the right of port 2-2'. On the left side of port 1-1' is the antenna, with an admittance of Y_a. In-between are the RTD parasitics: the top-contact resistance (r_c/A) and capacitance (Ac_c) and the spreading resistance (R_{spr}). (b) Sketch of a typical RTD mesa with its top-contact and spreading-resistance parasitics.

of single oscillators eventually clarifies the general performance limitations of the arrays.

The rest of this article is organized as follows. In Section II, we present an analysis framework and define an RTD-oscillator equivalent circuit, which is used in the subsequent analysis. In Section III, we provide details on the numerical simulation procedure. In Section IV, we describe the simulation results on the output power of RTD oscillators; a discussion is given in Section V. Finally, Section VI concludes this article.

II. Analysis Framework

An ac equivalent circuit of an RTD oscillator is sketched in Fig. 1(a). The oscillator consists of an RTD, a (lossy) antenna, and parasitic elements. This is a general equivalent circuit of an RTD oscillator, and any additional elements that may be present, such as impedance-matching circuitry or an additional resonator/radiator, can be simply considered a part of the antenna equivalent circuit. The RTD is the only nonlinear element in the circuit.

A. RTD Equivalent Circuit

To describe the nonlinear dynamic response of an RTD [particularly its negative differential conductance (NDC)], we apply a harmonic ac bias to it

$$V(t) = V_{\mathrm{dc}} + V_{\mathrm{ac}} \cos(\omega t) \tag{1}$$

where V_{dc} is the dc bias at the quiescent point, V_{ac} is the amplitude of the harmonic ac bias component, and ω is its angular frequency. In the RTD ac current, we retain only its first harmonic since higher harmonics are usually effectively short-circuited either by antenna or by RTD capacitance. Then, the specific RTD ac conductance ($g^{(1)}_{\mathrm{RTD}}$) and susceptance ($\omega c^{(1)}_{\mathrm{RTD}}$) are defined as the ratio of in-phase and quadrature first-harmonic components of the ac RTD current density and V_{ac}, where $c^{(1)}_{\mathrm{RTD}}$ is the specific (per unit area) RTD capacitance. The RTD ac admittance (Y_{RTD}) is

$$Y_{\mathrm{RTD}} = A g^{(1)}_{\mathrm{RTD}} + i\omega A c^{(1)}_{\mathrm{RTD}} \tag{2}$$

where A is the RTD-mesa area, and we represent Y_{RTD} with an RTD equivalent circuit in Fig. 1(a).

$g^{(1)}_{\mathrm{RTD}}$ and $c^{(1)}_{\mathrm{RTD}}$ are, in general, dependent on frequency, ac amplitude (V_{ac}), and on the dc quiescent point (V_{dc}). In the linear small-signal (SS) approximation, the frequency dependencies of $g_{\mathrm{RTD,SS}}(V_{\mathrm{dc}}, \omega)$ and $c_{\mathrm{RTD,SS}}(V_{\mathrm{dc}}, \omega)$ are governed by a certain tunnel charge-relaxation time (τ_{rel}) in RTDs; see details in [22], [23], [24], and [25]. An extension of this approach to accurately describe the nonlinear dependence on V_{ac} is detailed in [26]. However, we use a simplified approach in this article, as we did in [5]: we approximate $g^{(1)}_{\mathrm{RTD}}$ as

$$g^{(1)}_{\mathrm{RTD}}(V_{\mathrm{dc}}, \omega, V_{\mathrm{ac}}) = g^{(1)}_{\mathrm{RTD,dc}}(V_{\mathrm{dc}}, V_{\mathrm{ac}}) \frac{g_{\mathrm{RTD,SS}}(V_{\mathrm{dc}}, \omega)}{g_{\mathrm{RTD,SS}}(V_{\mathrm{dc}}, 0)} \tag{3}$$

where $g^{(1)}_{\mathrm{RTD,dc}}(V_{\mathrm{dc}}, V_{\mathrm{ac}})$ is the conductance calculated based on the dc RTD I–V curve; see details in [10], [27]. In such a way, the first term in (3) describes the nonlinear roll-off of the RTD conductance with V_{ac} based on the dc RTD I–V curve and the second SS term defines its roll-off with frequency. This approach guarantees a correct asymptotic behavior of $g^{(1)}_{\mathrm{RTD}}$ in both SS dynamic ($g^{(1)}_{\mathrm{RTD,dc}}(V_{\mathrm{dc}}, V_{\mathrm{ac}})|_{V_{\mathrm{ac}}\to 0} = g_{\mathrm{RTD,SS}}(V_{\mathrm{dc}}, 0)$) and large-signal quasi-static limits. A similar procedure is also applied to the calculation of RTD capacitance $c^{(1)}_{\mathrm{RTD}}(V_{\mathrm{dc}}, \omega, V_{\mathrm{ac}})$, defined via $c^{(1)}_{\mathrm{RTD,dc}}(V_{\mathrm{dc}}, V_{\mathrm{ac}})$ and $c_{\mathrm{RTD,SS}}(\omega)$ (see details in [5]).

The simplest model for the calculation of $g^{(1)}_{\mathrm{RTD,dc}}(V_{\mathrm{dc}}, V_{\mathrm{ac}})$ in (3) is based on a third-order polynomial approximation for the dc RTD I–V curve [10], [28], [29]. The approximation is usually defined by matching the peak and valley points of the real RTD I–V curve with a third-order polynomial (see examples in Fig. 2). Differentiating the third-order polynomial leads to a quadratic equation for the RTD NDC ($g^{(1)}_{\mathrm{RTD,3rd}}$ is quadratically decreasing with V_{ac}) [10], [28], [29]

$$g^{(1)}_{\mathrm{RTD,3rd}}(V_{\mathrm{ac}}) = g_{0,\mathrm{3rd}} \left(1 - \frac{V_{\mathrm{ac}}^2}{\Delta V^2}\right) \tag{4}$$

where ΔV is the dc peak-to-valley voltage difference, $g_{0,\mathrm{3rd}}$ is the NDC maximum for a third-order polynomial (see an illustration in Fig. 3). Now, we can revert (4) and express V_{ac}^2 as

$$V_{\mathrm{ac}}^2 = \Delta V^2 \left(1 - \frac{g^{(1)}_{\mathrm{RTD,3rd}}}{g_{0,\mathrm{3rd}}}\right). \tag{5}$$

This equation defines V_{ac}^2 as a function of $g^{(1)}_{\mathrm{RTD,3rd}}$ and it has a deep meaning. When an RTD is connected to a resonator (an oscillator circuit), $g^{(1)}_{\mathrm{RTD,3rd}}$ must be set equal (matched) to a loss conductance of an external (with respect to the RTD) oscillator circuit to fulfil oscillation conditions, as we discuss later (see

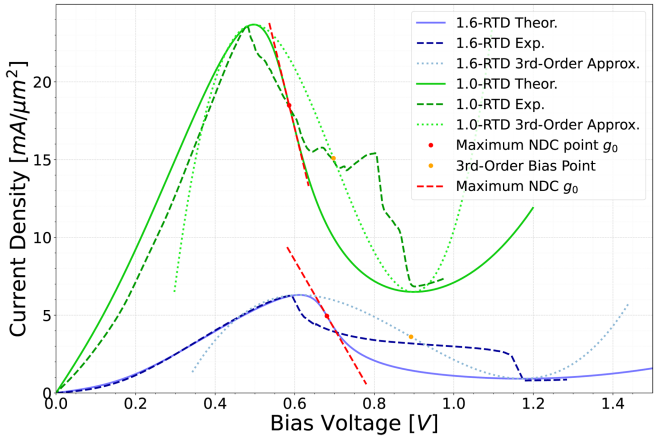

Fig. 2. Theoretical and experimental I–V curves for the two RTD wafers with 1.6 nm and 1.0 nm barriers discussed in this work. The third-order approximation and the maximum NDC for both curves are also shown.

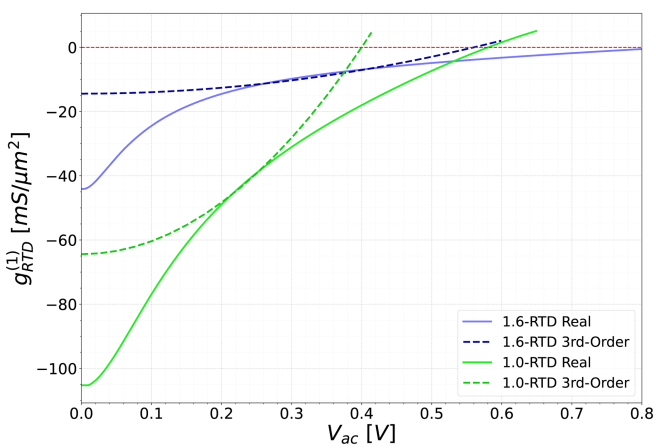

Fig. 3. DC RTD conductance as a function of $V_{\rm ac}$ for wafers 1.6-RTD and 1.0-RTD, third-order approximations are also shown.

Section II-D). In essence, this condition controls the RTD ac amplitude ($V_{\rm ac}$) in such a way that the RTD exhibits a properly matched (nonlinear) RTD conductance $g^{(1)}_{\rm RTD,3rd}$. We can introduce an external control parameter $\gamma = g^{(1)}_{\rm RTD,3rd}/g_{0,3\rm rd}$, which tells us how much the external-circuit conductance (which the RTD needs to match) is smaller than the maximum RTD NDC ($g_{0,3\rm rd}$). Then, we can rewrite (5) in a compact form $V^2_{\rm ac} = \Delta V^2(1-\gamma)$. Notice that $g^{(1)}_{\rm RTD,3rd}$ has to be negative in oscillators, i.e., $\gamma \geq 0$. In addition, if the external circuit imposes a $|g^{(1)}_{\rm RTD,3rd}|$, which is higher than $|g_{0,3\rm rd}|$ (i.e., $\gamma > 1$), then the RTD cannot provide it, its NDC is insufficient and the oscillations cannot be sustained. So, in any working oscillator, $\gamma \in [0, 1]$.

To illustrate graphically how the parameter γ defines $V_{\rm ac}$, we normalize $g^{(1)}_{\rm RTD,3rd}$ in Fig. 3 on $g_{0,3\rm rd}$, which gives us the parameter γ along y-axis. Then, we replace the x-axis with $V^2_{\rm ac}/\Delta V^2$ and finally flip the x and y axes in Fig. 3. Fig. 4 shows the result, graphically illustrates (5) and shows how the γ parameter defines $V_{\rm ac}$.

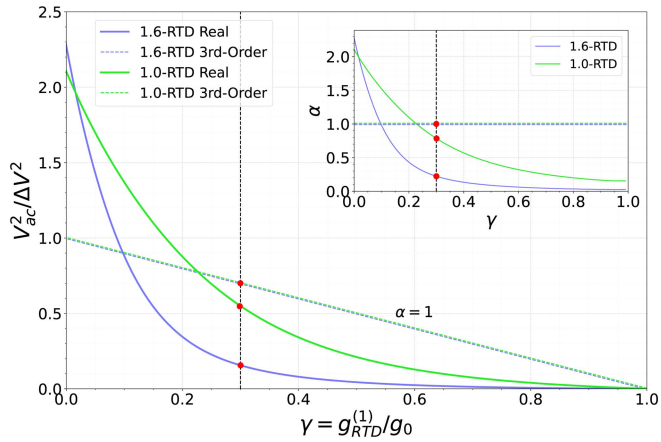

Fig. 4. Normalized ac amplitude ($V^2_{\rm ac}/\Delta V^2$) versus control parameter γ for 1.6- and 1.0-RTD wafers. The ratio between the normalized amplitude for a real RTD I–V curve (continuous lines) and its third-order approximation (dashed lines, $\alpha = 1$) corresponds to the correction coefficient α, as defined in (6). $\alpha(\gamma)$ for both RTD wafers is shown in the inset; notice the monotonous decrease of α with γ.

Now we note that the third-order approximation turns out to be quite rough: it typically underestimates the maximum RTD NDC by several times, considerably underestimates the maximum value of $V_{\rm ac}$ where RTD still exhibits NDC, and, in general, poorly approximates the actual RTD I–V curve in the NDC region [10] (see also examples in Figs. 2 and 3). Apart from that, it is by far not obvious how to reconcile a third-order approximation with a description of the frequency roll-off of the RTD NDC since the third-order approximation is merely a dc fitting, it is not based on a physical analysis of the (dynamic) tunnel processes in RTDs.

Therefore, we calculate $g^{(1)}_{\rm RTD,dc}(V_{\rm dc}, V_{\rm ac})$ based on a real RTD I–V curve and cast the result in a form similar to the third-order approximation with an additional correction coefficient α; see details in [10]. We start with the real RTD I–V curve, as the ones shown in Fig. 2. Then, we calculate the RTD conductance based on these curves for each $V_{\rm ac}$ at different RTD dc bias points ($V_{\rm dc}$) and define $g^{(1)}_{\rm RTD,dc}(V_{\rm ac})$ as the minima (largest NDC) found for each $V_{\rm ac}$. The procedure removes the explicit dependence of $g^{(1)}_{\rm RTD,dc}(V_{\rm ac})$ on $V_{\rm dc}$. The example curves in Fig. 3 show the result of this procedure. These are monotonous functions [10], similar to the curves discussed above for the third-order polynomial approximations. As a next step, we convert these curves to the format shown in Fig. 4. We can represent these numerically calculated curves in a simple form similar to (5) [10]

$$V^2_{\rm ac} = \Delta V^2\,(1-\gamma)\,\alpha(\gamma) \tag{6}$$

if we introduce a correction coefficient $\alpha(\gamma)$, describing the deviation of $V^2_{\rm ac}$ based on the real RTD I–V curves from that calculated with the third-order polynomial approximation (see Fig. 4); and if we redefine γ as

$$\gamma = \frac{g^{(1)}_{\rm RTD}(\omega, V_{\rm ac})}{g_0(\omega)} \tag{7}$$

TABLE I
MAIN PARAMETERS OF THE CONSIDERED RTD WAFERS

RTD wafers	1.6-RTD	1.0-RTD
Barrier thickness	1.6 nm	1.0 nm
ΔV	0.55 V	0.4 V
Peak current density	6.2 mA/μm^2	24 mA/μm^2
g_0 (dc)	−45 mS/μm^2	−105 mS/μm^2
$\tau_{\rm rel}$ (max NDC)	380 fs	85 fs
$\tau_{\rm RTD}(\omega)$ (with $c_{\rm RTD,SS}$)	≈400−550 fs	≈125−140 fs
$c_{\rm RTD,SS}(\omega)$	≈5−17 fF/μm^2	≈11−16 fF/μm^2

where $g_0(\omega)$ is defined as $g_{\rm RTD,SS}(V_{\rm dc},\omega)$ for $V_{\rm dc}$ at the maximum of NDC to take into account its frequency roll-off. If α is set equal to 1 and g_0 is the dc NDC maximum of the third-order approximation, then (6) corresponds exactly to the usual (dc) third-order approximation [29]. In the spirit of approximations of (3), equation (6) with γ defined by (7) is exact in the dc case and it also provides a correct SS limit at high frequencies, i.e., $V_{\rm ac}\to 0$, when $\gamma\to 1$. At high frequencies, the approximations given by (6) and (7) imply that the RTD I–V curves in Fig. 2 are getting compressed along the vertical axis proportionally to the reduction of RTD NDC with frequency ($g_0(\omega)$). Qualitatively, that seems to be a reasonable approximation, although, e.g., ΔV does change somewhat with frequency in reality [27].

We apply numerical simulations in this article to two RTD wafers with rather typical parameters for RTDs commonly found in the literature: one ("1.6-RTD") has thicker barriers of 1.6 nm and lower current density, the other one ("1.0-RTD") has thinner barriers of 1.0 nm and very high current density. We used these wafers in a number of experimental works [5], [10], [14], [30], [31]; one can find there also the layer sequences of the wafers and simulation details. The key parameters of the wafers are listed in Table I. Figs. 2 and 3 show the measured and simulated RTD I–V curves, their third-order approximations and the corresponding $g^{(1)}_{\rm RTD,dc}(V_{\rm ac})$ curves. As mentioned above, the plots clearly demonstrate large deviations between the third-order approximations and the actual characteristics.

B. Antenna and Parasitics

Now, we focus on the antenna and RTD parasitics in the equivalent circuit in Fig. 1(a). The RTD parasitics include the RTD top-contact and the spreading resistances. The latter one also includes the contribution of the RTD bottom contact [see schematic in Fig. 1(b)]. The typical value of the specific top-contact resistance ($\rho_{\rm c}$) for THz RTDs is in the range $\rho_{\rm c}=1-3\,\Omega\,\mu$m^2 (for sub-THz RTDs, one can also see larger values of $\rho_{\rm c}$ in the literature). The ohmic contacts also have a parallel capacitance, which, for RTDs, is at the level of ≈ 20 fF/μm^2. The corresponding RC time constant is $\approx 20-60$ fs. At 1 THz, that gives ωRC $\approx 0.1-0.4$, so the parasitics susceptance is negligibly small at frequencies below 1 THz and also below 2 THz for RTDs with very good contact resistance of $\rho_{\rm c}<1.5\,\Omega\,\mu$m^2. In the analytical formulas in this work, therefore, we assume that the RTD parasitics could be described only by their real resistance R_p [see Fig. 1(a)].

We start with a representation of the antenna admittance ($Y_{\rm a}$) in the form of an equivalent circuit shown in Fig. 1(a) and also

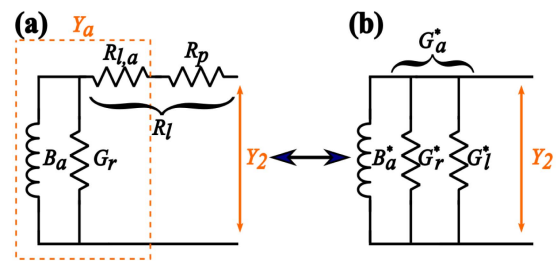

Fig. 5. (a) "Physical" and (b) parallel equivalent circuits for the antenna and RTD parasitics.

in Fig. 5(a), where B_a and G_r are the antenna susceptance and radiation conductance, respectively, and $R_{l,a}$ is the antenna ohmic-loss resistance. For a slot antenna, this mixed parallel–serial circuit is more physical compared to the more common parallel-circuit one, since each circuit parameter is more clearly linked to its physical origin: G_r is dependent on the slot length and should be only weakly dependent on the slot width; $R_{l,a}$ is roughly proportional to the slot circumference (slot length); B_a is defined by the slot dimensions. In addition, this equivalent circuit allows us to treat the antenna ohmic losses on an equal footing with the RTD parasitics. This is shown in Fig. 5(a), where parasitics and antenna losses are combined in a single lossy term $R_{\rm l}=R_{l,a}+R_p$.

Nevertheless, a parallel circuit is more convenient in the oscillator analysis, as it leads to simpler formulas. Therefore, as a next step, we convert the physical equivalent circuit of Fig. 5(a) to an equivalent parallel one in Fig. 5(b).

C. Transformation of Equivalent Circuit of Fig. 5(a) and (b)

We assume that B_a, G_r, and R_l in the equivalent circuit of Fig. 5(a) are known. Calculating the impedance $Z_2=1/Y_2$ from Fig. 5(a)

$$Z_2=R_l+\frac{1}{i\,B_a+G_r} \tag{8}$$

converting it to admittance Y_2, and taking the real and imaginary parts, we can write

$$B_a^*=\beta B_a \tag{9}$$

$$G_a^*=\beta\left[G_r+R_l\left(G_r^2+B_a^2\right)\right] \tag{10}$$

where $\beta\le 1$

$$\beta=\frac{1}{\left(1+R_lG_r\right)^2+\left(R_lB_a\right)^2}. \tag{11}$$

To split G_a^* into G_r^* and G_l^* in a unique way, we need to impose an additional condition on the radiated power being the same for the two circuits, i.e.,

$$G_r^*=\left|\frac{Y_2}{G_r+iB_a}\right|^2 G_r. \tag{12}$$

That leads to the definition of G_r^*

$$G_r^*=\beta G_r. \tag{13}$$

and $G_l = G_a - G_r$

$$G_l^* = \beta R_l \left(G_r^2 + B_a^2\right). \tag{14}$$

Now, all parameters in the equivalent circuit of Fig. 5(b) are uniquely defined.

D. RTD Oscillator

The oscillator circuit in Fig. 1(a) supports nontrivial solutions (with a nonzero ac amplitude) when the condition $Y_2 + Y_{\text{RTD}} = 0$ is satisfied [28]. This is a steady-state oscillation condition. Using the equivalent circuit in Fig. 5(b), we can rewrite this condition in the following form, separating its real and imaginary parts:

$$\begin{cases} g_{\text{RTD}}^{(1)} A &= -G_a^* \quad (15a) \\ \omega c_{\text{RTD}}^{(1)} A &= -B_a^*. \quad (15b) \end{cases}$$

Using (6), the output power (P) of an RTD oscillator can then be written as

$$P = \frac{1}{2} G_r^* V_{\text{ac}}^2 = \frac{1}{2} \Delta V^2 G_r^* (1-\gamma)\alpha(\gamma) \tag{16}$$

where γ is now linked to the antenna and parasitics parameters

$$\gamma = -\frac{G_a^*}{A g_0} = -\omega \tau_{\text{RTD}} \frac{G_a^*}{B_a^*} \tag{17}$$

where $\tau_{\text{RTD}} = -c_{\text{RTD}}^{(1)}/g_0$. For our RTDs, τ_{RTD} grows with frequency since $g_0(\omega)$ is decreasing with frequency faster than $c_{\text{RTD}}^{(1)}$; the value of τ_{RTD} in the frequency range up to 2 THz is specified in Table I.

Rewriting (16) and (17) in terms of the physical equivalent circuit parameters [see Fig. 5(a)], we get

$$P = \frac{1}{2} \Delta V^2 \beta G_r (1-\gamma)\alpha(\gamma) \tag{18}$$

$$\gamma = -\omega \tau_{\text{RTD}} \left[\frac{G_r}{B_a} + R_l \frac{G_r^2 + B_a^2}{B_a}\right]. \tag{19}$$

If we assume that

$$G_r \ll |B_a| \tag{20}$$

then

$$\gamma \approx -\omega \tau_{\text{RTD}} \left[\frac{G_r}{B_a} + R_l B_a\right] \tag{21}$$

and from (14)

$$G_l^* \approx \beta R_l B_a^2. \tag{22}$$

Condition (20) is usually well satisfied. Basically, it means that the antenna Q-factor with the account of only the antenna radiation losses is $Q = -B_a/G_r \gg 1$, which is justified as the slots used for RTD oscillators are usually operated in the regime of electrically small antennas.

Equation (18) indicates that to maximize P, one needs to make $\beta \approx 1$, maximize G_r, and minimize γ (α is monotonously decreasing with γ; see Fig. 4), ΔV has a fixed value for a given RTD wafer. For a symmetrical slot antenna (on InP), G_r grows monotonously with the slot length, and reaches a maximum of $G_{\text{r,res}} \approx 7$ mS at half-wavelength resonance. Correspondingly, the absolute upper bound for the oscillator output power is

$$P_{\text{max}} = \frac{1}{2} \Delta V^2 G_{\text{r,res}} \alpha(0). \tag{23}$$

P_{max} cannot be achieved in practice since the conditions $G_r = G_{\text{r,res}}$ and $\gamma = 0$ are not compatible: at resonance, $A \to 0$ and, according to (17), $\gamma \to \infty$. The actual limitations on P in an idealized case (no ohmic antenna losses and no RTD parasitics) we discussed in [10]. P is then maximized at specific optimal slot dimensions for a given RTD wafer and frequency. A simplified case with an account of ohmic antenna losses was discussed in [30]. According to (19), an account of losses leads to an increase of γ, reduction of P, and the optimal slot dimensions are consequently changing. This article is devoted to an analysis of a general case where all antenna losses and RTD parasitics are accurately taken into account.

III. Numerical Simulations of RTD Oscillators

As a next step, we need to define a complete set of parameters of an oscillator equivalent circuit. The RTD model we already defined in Section II-A. We add a stray capacitance of 0.3 fF in parallel to the antenna, which is usually present in fabricated oscillators. The RTD parasitics contain two contributions. One is the RTD top-contact resistance, equal to ρ_{c}/A. In the further simulations, we set $\rho_{\text{c}} = 2\,\Omega\,\mu\text{m}^2$. The second contribution is the spreading resistance, which we calculate based on the following set of parameters: RTD bottom-contact resistance is $10\,\Omega\,\mu\text{m}^2$ (with a contact capacitance of $20\,\text{fF}/\mu\text{m}^2$ in parallel) on top of 400 nm thick InGaAs (indium gallium arsenide) n++ layer with a doping of $5 \times 10^{19}\,\text{cm}^{-3}$. The total value of the spreading resistance is dependent on the RTD mesa area. In the definition of our model (see Fig. 1(a) and Section II-B), we took into account only the resistive part of the RTD parasitics ($R_p = \text{Re}(Z_{\text{p}})$). Our subsequent simulations confirmed that the account of their (neglected) imaginary part affects the output power of the optimized RTD oscillators by less than 8% (disregarding the cut-off region, where the difference is no more than $1\,\mu$W).

The remaining circuit parameters in Fig. 1(a) are related to the antenna. A schematic of a slot antenna of the oscillators we analyze in this article is shown in Fig. 6. To minimize the ohmic antenna losses (we aim for the maximum P), we choose an "island" design of the oscillator (see [5]). We take the conductance of evaporated gold layers to be equal to 2×10^5 S/cm, which is twice less than in bulk gold. When an idealized antenna without ohmic losses needs to be simulated, we assume the gold and silicon nitride (SiN) layers (see Fig. 6) to be ideally conducting. The RTD mesa was located at the very edge of the slot (no offset). High frequency simulation software by Ansys, Inc. (ANSYS HFSS) was used for the electromagnetic simulations of the antenna parameters. With the simulations, we generate a dataset for B_a, G_r, and $R_{l,a}$ at different frequencies covering the symmetrical slots with different lengths (l) and widths (w). l was changed from roughly one-sixth up to half-wavelength at the given frequency. w was changed from $1\,\mu$m (which is more or less the technological limit) up to $12\,\mu$m.

At each frequency, we, first, fix the slot parameters l and w; then, in a self-consistent loop, we look for a solution of (15a) and

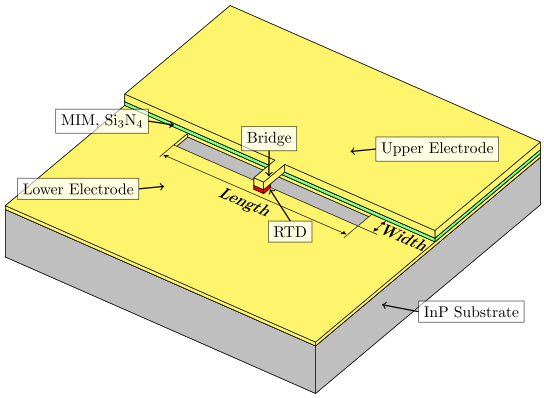

Fig. 6. Schematic of a slot-antenna RTD oscillator. The upper and lower electrodes are separated by a thin SiN layer, forming a metal-insulator-metal (MIM) capacitor. The lower electrode is lying directly on top of InP, with no n++ layer underneath, "island design" [5].

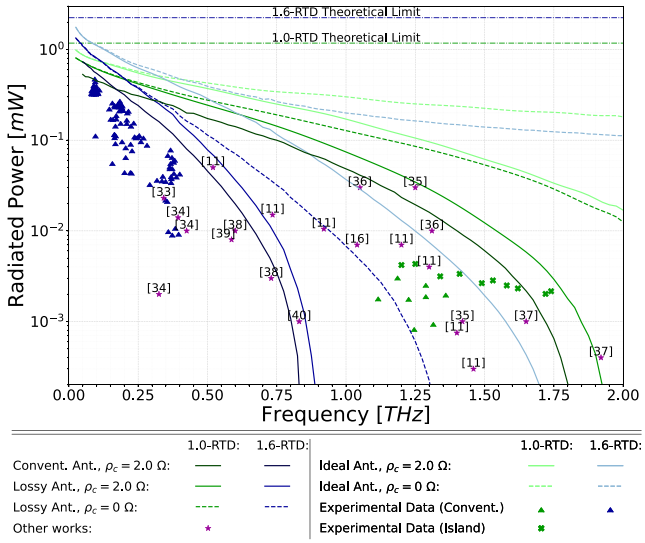

Fig. 7. Maximum output power for optimized symmetrical-slot-antenna RTD oscillators (island design [5]) for 1.6-RTD (blue lines) and 1.0-RTD (green lines) wafers in four cases. Case 1: ideal lossless RTD oscillators (dashed light-color lines). Case 2: ideal oscillator, but with an account of the top RTD contact (continuous light-color lines). Case 3: top-RTD-contact resistance is neglected, but all other losses and parasitics are taken into account (dashed dark lines). Case 4: all losses and parasitics are included (continuous dark lines). For comparison, we also show (with the darkest colors) the simulation results for conventional RTD oscillators (with an n++ layer under the lower electrode) with an account of all losses and parasitics. Green and blue triangles show experimental data (from [10], [30], [32], and some unpublished) for 1.6-RTD and 1.0-RTD wafers and conventional symmetrical-slot-antennas; green crosses show the corresponding data for the island design [5], [32]). The purple data points show literature data on symmetrical-slot-antenna RTD oscillators [11], [16], [33], [34], [35], [36], [37], [38], [39], [40].

(15b). If a solution is found, that gives us an RTD-mesa area (A), the value of the large-signal RTD capacitance $c^{(1)}_{\text{RTD}}(\omega, V_{\text{ac}})$, and V_{ac}. The power P is then calculated with (16). By scanning over l and w, we find the slot dimensions providing the maximum output power at any given frequency.

IV. Analysis of the Maximum Output Power

Following the procedure outlined above, we calculate the maximum output power in several cases for two RTD wafers (see Section II-A) and determine the corresponding optimum slot geometry and RTD-mesa size. The simulation results are shown in Fig. 7. Although we use the approximate equations (21) and (22) in several instances in the following (semi)quantitative discussion, all data plots are calculated without those approximations.

Case 1: We assume that the RTD and slot antenna are ideal, i.e., RTD has no contact parasitics and the antenna has no ohmic losses ($R_l = 0$), but the antenna radiates ($G_r \neq 0$). γ in this case [see (19)] is equal to

$$\gamma = \omega\tau_{\text{RTD}}\frac{G_r}{B_a} \tag{24}$$

which is shown in Fig. 8. To achieve higher power, γ should be minimized; therefore, the optimum slot has the minimum width ($w = 1\ \mu$m), since B_a increases with decrease of w, while G_r is largely unaffected by w and depends only on l. When $\omega \to 0$, γ in (24) goes to zero, and the output power approaches the absolute output-power maximum (P_{max}) discussed in [10], see also (23). This maximum is higher for 1.6-RTD with thicker barriers since it has a larger ΔV (that is not a general rule, but that applies to the RTD wafers analyzed by us here), $P_{\text{max}} \propto \Delta V^2$ (see [10]). At frequencies higher than ≈ 0.2 THz, 1.0-RTD provides higher output power than 1.6-RTD (see Fig. 7). With the increase in frequency, γ is increasing, but it remains $\ll 1$ beyond 2 THz. The output power in such an ideal case for both RTD wafers remains quite high up to 2 THz and beyond (see Fig. 7). Smaller τ_{RTD} for thin-barrier 1.0-RTD allows one to increase the antenna length (i.e., to make G_r larger), keeping $\gamma \ll 1$; therefore, the antenna length is closer to half wavelength and RTD area is smaller for 1.0-RTD (see Figs. 9 and 10).

Case 2: If we keep the slot lossless (except for G_r), but include the top-contact resistance of the RTDs, then we can simplify (21) for γ, using (9), (15a), and the relation $R_l = \rho_c/A$, valid in this case

$$\gamma \approx \omega\tau_{\text{RTD}}\left[\frac{G_r}{B_a} + \frac{\omega\tau_c}{\beta}\right] \tag{25}$$

where $\tau_c = c^{(1)}_{\text{RTD}}\rho_c$ is the top-RTD-contact RC time constant. According to (25), larger B_a reduces γ also in this case; therefore, w remains at its minimum level of 1 μm (see Fig. 11). The second term in the square brackets in (25) leads to a quadratic growth of γ at high frequencies (see Fig. 8). That leads to the appearance of a cut-off for the oscillation frequencies (where $\gamma = 1, \omega_{\text{cut-off}} \approx 1/\sqrt{\tau_c\tau_{\text{RTD}}}$; see [6]), although still at quite high frequencies for both RTD wafers, and to quite strong reduction of the maximum output power at high frequencies (see Fig. 7). Notice, close to the cut-off, the term G_r/B_a in (25) has to be ultimately minimized; therefore, l decreases that leads to reduction of G_r, increase of B_a, and, as a consequence, an increase of A at the cut-of (see Figs. 9 and 10).

At higher frequencies, the output power of 1.0-RTD is significantly higher than that of 1.6-RTD, which is a consequence of smaller τ_{RTD} and γ when the RTD barriers are thinner (see

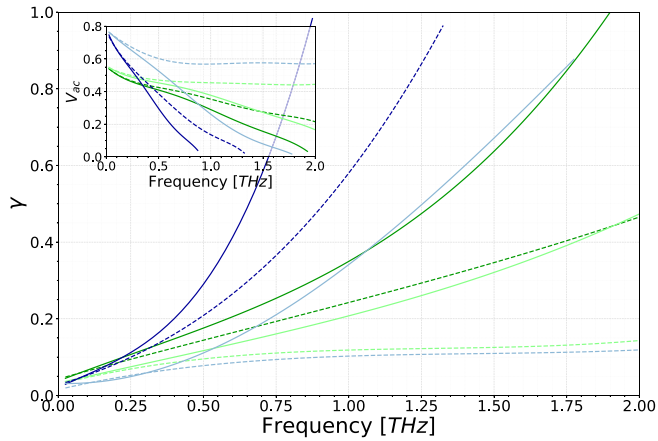

Fig. 8. γ versus frequency for optimized RTD oscillators; see notations in Fig. 7. The larger the parasitics, the faster γ approaches the cut-off value of 1, with γ for 1.0-RTD lying well below those for 1.6-RTD (when parasitics/losses are taken into account). The corresponding change of the ac amplitude for the two RTDs is shown in the inset.

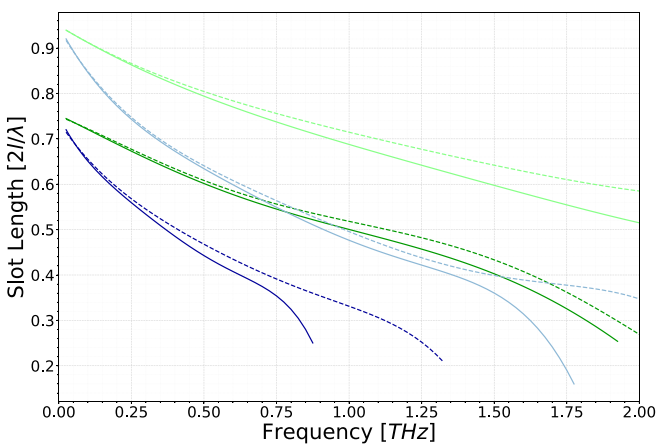

Fig. 9. Slot lengths normalized to effective half wavelength; see notations in Fig. 7.

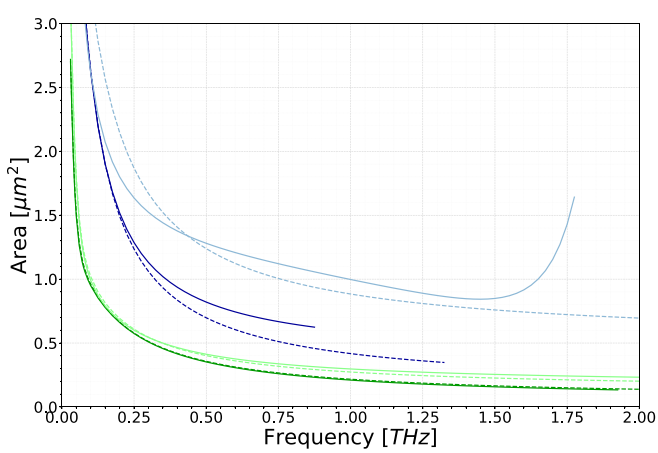

Fig. 10. RTD-mesa area; see notations in Fig. 7. Notice the sharp decrease in the area at the lowest frequencies and the convergence to a finite value at the cut-off (except for an idealized case 2).

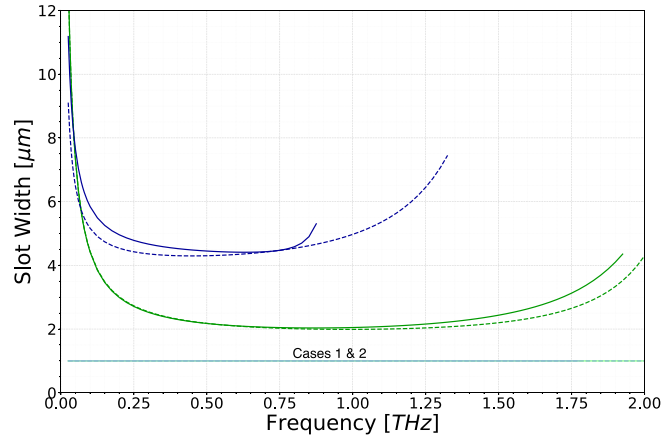

Fig. 11. Slot widths for optimized RTD oscillators; see notations in Fig. 7.

Figs. 7 and 8). The optimal RTD area remains close to that in the ideal case 1 (see Fig. 10).

Case 3: Now, we illustrate the ultimate performance of RTD oscillators if the top RTD contact is ideal. We include the antenna ohmic losses and keep the RTD spreading resistance but set $\rho_c = 0$. In this case, we can rewrite (21) in the form

$$\gamma \approx \omega\tau_{\text{RTD}} \left[\frac{G_r}{B_a} + B_a \left(R_{l,a} + R_{\text{spr}}\right)\right] \tag{26}$$

where we replaced R_l with $R_{l,a} + R_{\text{spr}}$. Looking at the plots for P and γ in Fig. 7, we can see that P is strongly reduced compared to the ideal case 1 and even to case 2 (for 1.6-RTD). In addition, Figs. 7 and 8 show a dramatic advantage of thin-barrier 1.0-RTD at THz frequencies: cut-off frequency well beyond 2 THz (contrary to ≈ 1.3 THz for 1.6-RTD) and much higher output-power level.

We notice the following traits in the changes of the oscillator parameters. When losses $R_{l,a} + R_{\text{spr}}$ are introduced, γ in (26) is increasing. Two things are happening to mitigate this increase. First, the slot is getting wider (see Fig. 11) since B_a drops with w. That leads to the reduction of the second term in the square brackets in (26). Notice that the reduction of B_a also leads to the reduction of the RTD-mesa area A (see Fig. 10). Second, with the reduction of B_a, the first term in the square brackets in (26) is increasing, the term was dominant in the ideal case 1. To mitigate that, the antenna is getting shorter; see Fig. 9, since $G_r \propto l^2$. A certain optimal value for l should be found, to maximize P. All these changes in the oscillator parameters are happening to reduce, to a certain extent, γ and, eventually, to maximize P.

Case 4: Now, we include all contributions to antenna ohmic losses and all RTD parasitics (see Figs. 7–10). An approximate equation for γ now combines the contributions considered separately in (25) and (26)

$$\gamma \approx \omega\tau_{\text{RTD}} \left[\frac{G_r}{B_a} + B_a \left(R_{l,a} + R_{\text{spr}}\right) + \frac{\omega\tau_c}{\beta}\right]. \tag{27}$$

The additional (compared to case 3) top-contact-resistance term in (27) leads to a significant increase of γ and reduction of the

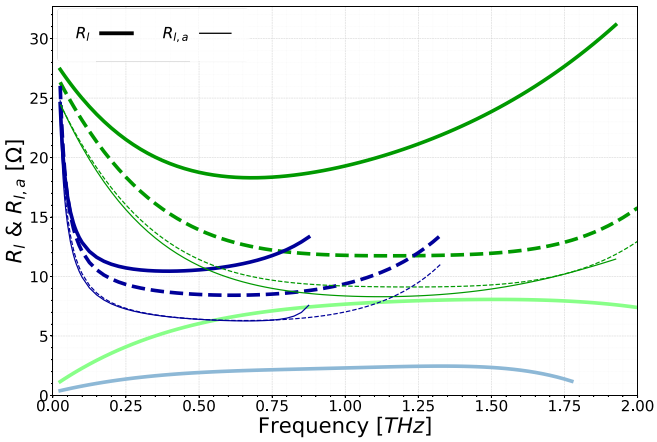

Fig. 12. Series resistances R_l and $R_{l,a}$ as in the circuit in Fig. 5(a); the notations for the curves are the same, as in Fig. 7, thicker lines show R_l while thinner ones represent $R_{l,a}$.

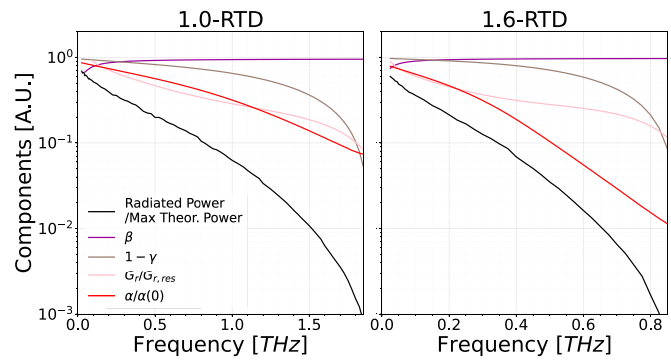

Fig. 13. P normalized on $P_{\max}$ and the constituting terms β, $G_r/G_{r,\text{res}}$, $1-\gamma$, and $\alpha(\gamma)/\alpha(0)$ [see (18) and (23)] for 1.0-RTD and 1.6-RTD.

output power at higher frequencies (see Figs. 7 and 8). As a result, 1.0-RTD gets cut-off at the frequency of ≈ 1.9 THz, and the cut-off frequency of 1.6-RTD reduces to ≈ 0.85 THz (compared to case 3). The optimal slot length and RTD mesas remain close to those we have seen in case 3 (see Figs. 9 and 10) except in the proximity of the cut-off, where the last term in the square brackets, related to the top contact, becomes relevant, ultimately leading to a lower cut-off frequency and lower output power.

To give a feeling of the scale of different loss resistances, we show $R_{l,a}$ and R_l in Fig. 12 for cases 2–4. One can see that $R_{l,a}$ is in the range $\sim 7-10\,\Omega$ at frequencies $\gtrsim 0.5$ THz and $\gtrsim 0.1$ THz for optimized 1.0- and 1.6-RTD oscillators, respectively. R_{spr} (see the offset between the thick and thin dashed lines, case 3) remains significantly smaller than $R_{l,a}$. The contribution of the RTD top-contact resistance is getting particularly significant (due to small RTD areas) for optimized 1.0-RTD oscillators, where it grows from $\sim 5\,\Omega$ to $\sim 20\,\Omega$ at frequencies $\gtrsim 0.5$ THz: it is seen roughly as an offset between the thick continues and dashed lines. The contribution of the top-contact resistance in 1.6-RTDs below the cut-off frequency is less dramatic.

To get more insight into the interplay of different factors having an influence on the output power of the RTD oscillators, we plot P normalized on $P_{\max}$ [see (18) and (23)] and different terms, determining this ratio, in Fig. 13.

Fig. 13 shows that, for optimized RTD oscillators, β, a power-divider term (11), has almost no or little impact at high sub-THz and THz frequencies. However, at lower frequencies, where the antennas are longer, its value decreases and becomes less than 0.9 below 100 GHz for 1.6-RTD and below 300 GHz for 1.0-RTD [see (11)]. $1-\gamma$ has a significant impact on the power reduction, but the largest contribution is coming from the $G_r/G_{\text{r,res}}$ and $\alpha(\gamma)$ terms. The term $\alpha(\gamma)$ is related to the actual shape of the RTD I–V curve and its deviation from a simplified third-order polynomial approximation. The impact of the term $\alpha(\gamma)$ is especially strong for the 1.6-RTD wafer (see Fig. 13), where the NDC region is quite steep, and the deviation from third-order approximation is particularly large (see Fig. 2).

V. Discussion

The data shown in Fig. 7 elucidate the role of different loss mechanisms in the limitation of the output power of symmetrical-slot-antenna RTD oscillators. As a reference, we take the ideal RTD oscillators (case 1). Surprisingly, such oscillators should provide quite high output power of $\sim 100\,\mu$W beyond 2 THz, and even the low-current-density 1.6-RTD wafer should perform at the same level as 1.0-RTD.

Furthermore, cases 2 and 3 illustrate the relative roles of the top-RTD-contact resistance versus the "other loss mechanisms." Looking at the data for 1.0-RTD, we can see that the "other loss mechanisms" (case 3) give a major contribution to the reduction of the output power at sub-THz frequencies. At frequencies above ≈ 1 THz, the contribution of both mechanisms to the reduction of power becomes more or less similar, with the "other loss mechanisms" slightly dominating though. The role of the "other loss mechanisms" is significantly more dramatic for the 1.6-RTD wafer: the "other loss mechanisms" cause almost an order of magnitude higher power loss at sub-THz and THz frequencies than the top-RTD-contact resistance. The presented data and abovementioned observations indicate that the top-RTD-contact resistance is not the major mechanism of the output-power limitation in RTD oscillators; the situation is more nuanced.

Nevertheless, when we compare the realistic RTD oscillators and those without the top-RTD-contact resistance (case 4 versus 3), we see a dramatic impact of the top-RTD-contact resistance at the high end of the oscillator operating frequencies: the output power could be increased by an order of magnitude (and more), and the cut-off frequency could be greatly increased, if the top-RTD-contact resistance could have been eliminated or reduced. The top-RTD-contact resistance does play a crucial role in those regimes.

Referring to the general case 4, a major loss mechanism can hardly be identified since an RTD oscillator is a complicated system with an intricate interplay between different loss mechanisms with different time constants, e.g., τ_{RTD}, τ_{rel}, τ_{c}, internal antenna RL time constant. These time constants usually have comparable values, and that partly also explains the difficulty in singling out a major loss mechanism. On top of that, P depends in a complicated way on all these time constants, other

parameters [see (18)], the shape of the I–V curve, etc. We have also replotted Fig. 7 in a log–log scale. One could expect a piece-wise linear characteristic with a clearly distinguishable kink at a corner frequency if there would be a major mechanism responsible for the power decrease. However, the curves exhibit a continuously accelerating decrease with frequency without piece-wise linear sections and identifiable kinks. That also indicates that a dominant loss mechanism is not identifiable in RTD oscillators, at least in those with symmetrical slot antennas.

Nevertheless, our simulation data reproduce the generally observed trend in the reduction of the output power of simple symmetrical-slot-antenna RTD oscillators: ≈ 0.5 mW at ≈ 100 GHz, some tens of μW at ≈ 1 THz, and $\sim$ μW at ~ 2 THz. Our data also show that the frequency roll-off of the output power is dramatically faster for RTDs with thicker barriers and low current density. In particular, the thin-barrier high-current-density RTDs not only have a higher cut-off and higher output power at the THz frequencies, but they can provide much higher output power (compared to 1.6-RTD) also at the sub-THz frequencies. RTDs of 1.0-RTD type allow for the operation of an RTD oscillator in a more optimal regime: lower γ, longer l, larger G_r. This observation contradicts the statement that low-current-density RTDs can provide good performance at sub-THz frequencies. Although 1.6-RTD shows a higher output power compared to 1.0-RTD at very low sub-THz frequencies in Fig. 7 that is not a general trait; it is related to larger ΔV in our specific example RTDs. ΔV is an independent RTD design parameter and it is not inherently related to RTD current density.

Intuitively, one would expect that with the increase of the antenna losses, the RTD-mesa area should grow to provide more gain to the oscillator to compensate for the losses. However, Fig. 10 shows the opposite trait when we compare cases 1 and 2 with 3 and 4: an optimal RTD-mesa area is shrinking when antenna ohmic losses are included. As we mentioned above in Section IV that is related to the increase of the slot width and reduction of B_a with the increase of antenna losses.

Fig. 10 shows another quite surprising outcome of our analysis: the RTD-mesa area remains around 0.1 μm^2 for the optimized RTD oscillators. 0.1 μm^2 is still within the reach of the common e-beam-lithography fabrication process for RTD oscillators, although it is close to its limit. Therefore, RTD-mesa areas of RTD oscillators optimized for maximum power are within an acceptable range for fabrication technology.

To verify the correlation of our simulations and experiment, we show a large number of experimental data points in Fig. 7, obtained with 1.6-RTD and 1.0-RTD wafers. All experimental data are in good agreement with our calculations of the maximum output power in optimized oscillators: all data points lie below the optimum curves, but some (with close-to-optimum parameters) almost reach them. Island-design oscillators have been studied experimentally only with 1.0-RTDs so far [5]). On the other hand, the experimental data on conventional oscillators (with n++ layer under the lower electrode) were mostly obtained with 1.6-RTDs [10], [30], although some limited data with 1.0-RTDs are also available [32]). For conventional RTD oscillators, the antenna ohmic loss is higher, which results in lower output power. To illustrate that, we also show the simulation results for conventional RTD oscillators in Fig. 7; their output power is approximately twice lower than that for the island design.

The available literature data on symmetrical-slot-antenna RTD oscillators are also plotted in Fig. 7. The RTD wafers in those publications had parameters somewhere in between our 1.6-RTD and 1.0-RTD wafers. Sometimes, the RTD current density is somewhat higher than that in our 1.0-RTD wafer. Our simulation data for the 1.0-RTD wafer describes reasonably well the upper bound for the output power reported in the literature.

VI. Conclusion

The presented data let us draw the following conclusions for symmetrical-slot-antenna RTD oscillators.

1) An ideal lossless RTD oscillator would work at multi-THz frequencies with a high output power ($\sim 100\,\mu$W) even with RTDs with relatively thick barriers (1.6-RTD).
2) However, well in agreement with available experimental data, the frequency limit of realistic oscillators with high-current-density RTDs (1.0-RTD), nearly ultimately reduced parasitics ($\rho_c \approx 2\,\Omega\,\mu$m^2) and antenna losses (island design) is around 2 THz, with the output power continuously decreasing from ~ 0.5 mW at low frequencies to $\sim 1\,\mu$W at the upper frequency end.
3) The frequency roll-off of the output power has a complicated form related to the RTD contact parasitics, ohmic antenna losses, antenna geometry, shape of the RTD I–V curve, and RTD barrier thickness (RTD time constants). All these parameters have a crucial impact on the frequency roll-off.
4) The top-RTD-contact resistance has a crucial impact on the output power of the oscillators at the high end of their operating range and on their cut-off frequency.
5) The use of high-current-density RTDs is crucial to achieve high output power at THz but also at sub-THz frequencies. Oscillators with low-current-density RTDs exhibit much steeper frequency roll-off.
6) The required minimum RTD-mesa area for optimized oscillators at frequencies $\approx 1-2$ THz is in the range $\approx 0.1-0.2\,\mu$m^2, which the common RTD-fabrication technology can cover.

The abovementioned traits are likely to be (at least qualitatively) applicable to other types of RTD oscillators.

References

[1] S. S. Dhillon et al., "The 2017 terahertz science and technology roadmap," *J. Phys. D: Appl. Phys.*, vol. 50, 2017, Art. no. 043001, doi: 10.1088/1361-6463/50/4/043001.

[2] E. Bründermann, H. W. Hübers, and M. F. Kimmitt, *Terahertz Techniques*. Berlin, Germany: Springer, 2012.

[3] E. R. Brown et al., "Oscillations up to 712 GHz in InAs/AlSb resonant-tunneling diodes," *Appl. Phys. Lett.*, vol. 58, 1991, Art. no. 2291, doi: 10.1063/1.104902.

[4] R. Izumi, S. Suzuki, and M. Asada, "1.98 THz resonant-tunneling-diode oscillator with reduced conduction loss by thick antenna electrode," in *Proc. 42nd Int. Conf. Infrared, Millim., Terahertz Waves (IRMMW-THz)*, 2017, pp. 1–2, doi: 10.1109/IRMMW-THz.2017.8066877.

[5] D. Tuan Nguyen, P. Ourednik, and M. Feiginov, "Island THz on-chip slot-antenna resonant-tunneling-diode oscillators," *Appl. Phys. Lett.*, vol. 123, no. 4, 2023, Art. no. 043508, doi: 10.1063/5.0159147.

[6] M. Feiginov, "Frequency limitations of resonant-tunnelling diodes in Sub-THz and THz oscillators and detectors," *J. Infrared, Millim., THz Waves*, vol. 40, pp. 365–394, 2019, doi: 10.1007/s10762-019-00573-5.

[7] M. Asada and S. Suzuki, "Terahertz emitter using resonant-tunneling diode and applications," *Sensors*, vol. 21, no. 4, 2021, Art. no. 1384, doi: 10.3390/s21041384.

[8] X. B. Mei et al., "First demonstration of amplification at 1 THz using 25-nm InP high electron mobility transistor process," *IEEE Electron Dev. Lett.*, vol. 36, pp. 327–329, Apr. 2015, doi: 10.1109/LED.2015.2407193.

[9] M. Urteaga, Z. Griffith, M. Seo, J. Hacker, and M. J. W. Rodwell, "InP HBT technologies for THz integrated circuits," *Proc. IEEE*, vol. 105, no. 6, pp. 1051–1067, Jun. 2017, doi: 10.1109/JPROC.2017.2692178.

[10] C. Spudat, P. Ourednik, G. Picco, D. T. Nguyen, and M. Feiginov, "Limitations of output power and efficiency of simple resonant-tunneling-diode oscillators," *IEEE Trans. THz Sci. Technol.*, vol. 13, no. 1, pp. 82–92, Jan. 2023, doi: 10.1109/TTHZ.2022.3228069.

[11] M. Feiginov, H. Kanaya, S. Suzuki, and M. Asada, "Operation of resonant-tunneling diodes with strong back injection from the collector at frequencies up to 1.46 THz," *Appl. Phys. Lett.*, vol. 104, 2014, Art. no. 243509, doi: 10.1063/1.4884602.

[12] H. Kanaya, T. Maekawa, S. Suzuki, and M. Asada, "Structure dependence of oscillation characteristics of resonant-tunneling-diode terahertz oscillators associated with intrinsic and extrinsic delay times," *Jpn. J. Appl. Phys.*, vol. 54, no. 9, 2015, Art. no. 094103, doi: 10.7567/JJAP.54.094103.

[13] K. Kasagi, S. Suzuki, and M. Asada, "Large-scale array of resonant-tunneling-diode terahertz oscillators for high output power at 1 THz," *J. Appl. Phys.*, vol. 125, no. 15, 2019, Art. no. 151601, doi: 10.1063/1.5051007.

[14] P. Ourednik and M. Feiginov, "Double-resonant-tunneling-diode bridgeless patch-antenna oscillators operating up to 1.09 THz," *Appl. Phys. Lett.*, vol. 120, no. 18, Art. no. 183501, 2022, doi: 10.1063/5.0090519.

[15] M. Reddy et al., "Monolithic Schottky-collector resonant tunnel diode oscillator arrays to 650 GHz," *IEEE Electron Dev. Lett.*, vol. 18, no. 5, pp. 218–221, May 1997, doi: 10.1109/55.568771.

[16] S. Suzuki, M. Asada, A. Teranishi, H. Sugiyama, and H. Yokoyama, "Fundamental oscillation of resonant tunneling diodes above 1 THz at room temperature," *Appl. Phys. Lett.*, vol. 97, 2010, Art. no. 242102, doi: 10.1063/1.3525834.

[17] M. Shiraishi et al., "High output power (400 μW) oscillators at around 550 GHz using resonant tunneling diodes with graded emitter and thin barriers," *Appl. Phys. Exp.*, vol. 4, no. 6, 2011, Art. no. 064101, doi: 10.1143/APEX.4.064101.

[18] M. Kim, J. Lee, J. Lee, and K. Yang, "A 675 GHz differential oscillator based on a resonant tunneling diode," *IEEE Trans. THz Sci. Technol.*, vol. 6, no. 3, pp. 510–512, May 2016, doi: 10.1109/TTHZ.2016.2554399.

[19] T. Van Mai, M. Asada, T. Namba, Y. Suzuki, and S. Suzuki, "Coherent power combination in a resonant-tunneling-diode arrayed oscillator with simplified structure," *IEEE Trans. THz Sci. Technol.*, vol. 13, no. 4, pp. 405–414, Jul. 2023, doi: 10.1109/TTHZ.2023.3270672.

[20] S. Iwamatsu, Y. Nishida, M. Fujita, and T. Nagatsuma, "Terahertz coherent oscillator integrated with slot-ring antenna using two resonant tunneling diodes," *Appl. Phys. Exp.*, vol. 14, no. 3, 2021, Art. no. 034001, doi: 10.35848/1882-0786/abdb8f.

[21] Y. Koyama et al., "A high-power terahertz source over 10 mW at 0.45 THz using an active antenna array with integrated patch antennas and resonant-tunneling diodes," *IEEE Trans. THz Sci. Technol.*, vol. 12, no. 5, pp. 510–519, Sep. 2022, doi: 10.1109/TTHZ.2022.3180492.

[22] M. Feiginov, "Effect of the coulomb interaction on the response time and impedance of the resonant-tunneling diodes," *Appl. Phys. Lett.*, vol. 76, 2000, Art. no. 2904, doi: 10.1063/1.126512.

[23] M. N. Feiginov, "Does the quasibound-state lifetime restrict the high-frequency operation of resonant-tunnelling diodes?," *Nanotechnol.*, vol. 11, no. 4, 2000, Art. no. 359, doi: 10.1088/0957-4484/11/4/333.

[24] M. N. Feiginov, "Displacement currents and the real part of high-frequency conductance of the resonant-tunneling diode," *Appl. Phys. Lett.*, vol. 78, 2001, Art. no. 3301, doi: 10.1063/1.1372357.

[25] M. Feiginov and D. Roy Chowdhury, "Operation of resonant-tunneling diodes beyond resonant-state-lifetime limit," *Appl. Phys. Lett.*, vol. 91, 2007, Art. no. 203501, doi: 10.1063/1.2806922.

[26] P. Ourednik, G. Picco, D. Tuan Nguyen, C. Spudat, and M. Feiginov, "Large-signal dynamics of resonant-tunneling diodes," *J. Appl. Phys.*, vol. 133, no. 1, 2023, Art. no. 014501, doi: 10.1063/5.0134223.

[27] M. Feiginov, C. Sydlo, O. Cojocari, and P. Meissner, "High-frequency nonlinear characteristics of resonant-tunneling diodes," *Appl. Phys. Lett.*, vol. 99, 2011, Art. no. 233506, doi: 10.1063/1.3644491.

[28] C. Kim and A. Brändli, "High-frequency high-power operation of tunnel diodes," *IRE Trans. Circuit Theory*, vol. 8, 1961, Art. no. 416, doi: 10.1109/TCT.1961.1086849.

[29] M. Asada, S. Suzuki, and N. Kishimoto, "Resonant tunneling diodes for sub-terahertz and terahertz oscillators," *Jpn. J. Appl. Phys.*, vol. 47, no. 6, pp. 4375–4384, 2008, doi: 10.1143/JJAP.47.4375.

[30] D. T. Nguyen, G. Picco, P. Ourednik, C. Spudat, and M. Feiginov, "Impact of slot width on performance of symmetrical-slot-antenna resonant-tunneling-diode oscillators," *IEEE Trans. THz Sci. Technol.*, vol. 14, no. 1, pp. 29–38, Jan. 2024, doi: 10.1109/TTHZ.2023.3329460.

[31] P. Ourednik, T. Hackl, C. Spudat, D. Tuan Nguyen, and M. Feiginov, "Double-resonant-tunneling-diode patch-antenna oscillators," *Appl. Phys. Lett.*, vol. 119, no. 26, 2021, Art. no. 263509, doi: 10.1063/5.0068114.

[32] D. T. Nguyen, P. Ourednik, and M. Feiginov, "Conventional vs. island THz slot-antenna resonant-tunneling-diode oscillators," in *Proc. 48th Int. Conf. Infrared, Millimeter, Terahertz Waves (IRMMW-THz)*, 2023, pp. 1–2, doi: 10.1109/IRMMW-THz57677.2023.10298944.

[33] N. Orihashi, S. Suzuki, and M. Asada, "One THz harmonic oscillation of resonant tunneling diodes," *Appl. Phys. Lett.*, vol. 87, 2005, Art. no. 233501, doi: 10.1063/1.2139850.

[34] N. Kishimoto, S. Suzuki, A. Teranishi, and M. Asada, "Frequency increase of resonant tunneling diode oscillators in Sub-THz and THz range using thick spacer layers," *Appl. Phys. Exp.*, vol. 1, 2008, Art. no. 042003, doi: 10.1143/APEX.1.042003.

[35] H. Kanaya, R. Sogabe, T. Maekawa, S. Suzuki, and M. Asada, "Fundamental oscillation up to 1.42 THz in resonant tunneling diodes by optimized collector spacer thickness," *J. Infrared, Millimeter, THz Waves*, no. 35, p. 425–431, 2014, doi: 10.1007/s10762-014-0058-z.

[36] H. Kanaya, H. Shibayama, R. Sogabe, S. Suzuki, and M. Asada, "Fundamental oscillation up to 1.31 THz in resonant tunneling diodes with thin well and barriers," *Appl. Phys. Exp.*, vol. 5, no. 12, p. 425–431, 2012, doi: 10.1143/APEX.5.124101.

[37] T. Maekawa, H. Kanaya, S. Suzuki, and M. Asada, "Oscillation up to 1.92 THz in resonant tunneling diode by reduced conduction loss," *Appl. Phys. Exp.*, vol. 9, 2016, Art. no. 024101, doi: 10.7567/APEX.9.024101.

[38] T. Van Mai, Y. Suzuki, Y. Xiongbin, S. Suzuki, and M. Asada, "Structure-simplified resonant-tunneling-diode terahertz oscillator without metal-insulator-metal capacitors," *J. Infrared, Millim., THz Waves*, vol. 41, pp. 1498–1507, 2020, doi: 10.1007/s10762-020-00738-7.

[39] N. Orihashi, S. Hattori, S. Suzuki, and M. Asada, "Experimental and theoretical characteristics of sub-terahertz and terahertz oscillations of resonant tunneling diodes integrated with slot antennas," *Jpn. J. Appl. Phys.*, vol. 44, 2005, Art. no. 7809, doi: 10.1143/JJAP.44.7809.

[40] S. Suzuki et al., "Fundamental oscillation of up to 831 GHz in GaInAs/AlAs resonant tunneling diode," *Appl. Phys. Exp.*, vol. 2, 2009, Art. no. 054501, doi: 10.1143/APEX.2.054501.

Gabriele Picco received the B.Sc. and M.Sc. degrees in physics from the Universitá degli studi di Trieste, Trieste, Italy, in 2016 and 2019, respectively. Since 2021, he has been working toward the Ph.D. degree in electrical engineering with the Technische Universität Wien, Vienna, Austria.

His research interests include semiconductor physics and THz electronics.

Petr Ourednik received the B.E. and M.E. degrees in electrical engineering from the Czech Technical University, Prague, Czech Republic, in 2014 and 2016, respectively, and the Ph.D. degree in electrical engineering from the Technische Universität Wien, Vienna, Austria, in 2023.

From 2016 to 2018, he was with the Czech Technical University, Prague, Czech Republic, as a Research Associate. Since 2018, he has been with the Technische Universität Wien, Vienna, Austria. His research interests include high-frequency and THz electronics.

Dinh Tuan Nguyen received the B.E. and M.E. degrees in electrical engineering from the Moscow Institute of Physics and Technology, Moscow, Russia, in 2010 and 2012, respectively, and the Ph.D. degree in electrical engineering from the Technische Universität Wien, Vienna, Austria, in 2023.

From 2013 to 2019, he was with Le Quy Don Technical University, Hanoi, Vietnam, as a Teaching Assistant and Lecturer. Since 2018, he was with the Technische Universität Wien, Vienna, Austria. Since 2023, he is with Le Quy Don Technical University, Hanoi, Vietnam. His research interests include THz electronics.

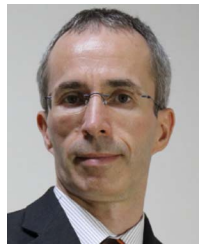

Michael Feiginov received the M.Sc. degree in electrical engineering and physics from the Moscow Institute of Physics and Technology, Moscow, Russia, in 1994 and the Ph.D. degree in physics of semiconductors and dielectrics from the Institute of Radioengineering and Electronics, Russian Academy of Sciences, Moscow, Russia, in 1999.

From 1994 to 2000, he was with the Institute of Radioengineering and Electronics, Russian Academy of Sciences, as a Junior Scientist, Scientist, and Senior Scientist. In 2001, he was with the Technische Universität Chemnitz, Chemnitz, Germany, as a Researcher. From 2002 to 2013, he was with the Technische Universität Darmstadt, Darmstadt, Germany, as a Senior Researcher. From 2013 to 2014, he was with the Tokyo Institute of Technology, Tokyo, Japan, as a Visiting Researcher. From 2014 to 2016, he was with Canon Inc., Tokyo, Japan, as a Scientific Manager with Frontier Research Center. Since 2016, he has been a Professor with Technische Universität Wien, Vienna, Austria. His research interests include THz electronics and photonics.